

# An AFM Study of the Correlation of Lead Dioxide Electrocatalytic Activity with Observed Morphology

Michael E. Hyde, Robert M. J. Jacobs, and Richard G. Compton\*

Physical and Theoretical Chemistry Laboratory, University of Oxford,  
South Parks Road, Oxford, OX1 3QZ, United Kingdom

Received: November 21, 2003; In Final Form: March 8, 2004

PbO<sub>2</sub> is widely employed as an electrocatalyst for anodic oxidation processes including the generation of oxygen and the degradation of various organic species in aqueous solution. However, despite extensive investigation, the precise mechanism of action remains obscure. In this paper we establish a previously unrecognized strong correlation between the morphology of the PbO<sub>2</sub> deposits and their electrocatalytic activity. Cyclic voltammetric results are described for the electrodeposition of PbO<sub>2</sub> on boron-doped diamond (BDD) electrodes from 2.5 mM solutions of lead(II) nitrate in nitric acid at pH values between approximately 0 and 7. A likely change in mechanism is observed around pH 4, consistent with the Pourbaix diagram of lead. The morphology of the PbO<sub>2</sub> films is observed as a function of time and potential, using in situ AFM in each of the lead solutions. Information on the growth rates of the films is extracted, and the limitations of using AFM in such an application are discussed. It is shown that the deposit morphology depends strongly on the specific conditions used. The oxidation of a 100 mM glucose solution on electrodes modified by PbO<sub>2</sub> deposition at a range of potentials and pH values is used as an indicator of the catalytic activity of the corresponding films, leading to the observation of the correlation between deposit morphology and catalytic activity mentioned above.

## Introduction

The electrodeposition of lead dioxide on carbon electrodes is currently of interest owing to the good electrical conductivity, favorably high potential for oxygen evolution, and chemical inertness of PbO<sub>2</sub>. These properties suggest applications in a variety of fields, notably the generation of oxygen and ozone<sup>1,2</sup> and electrooxidation of organic compounds. The latter has been used in both synthesis<sup>3–6</sup> and degradation (for example of organic contaminants in wastewater).<sup>7–9</sup>

Relatively few studies of the deposition of PbO<sub>2</sub> on to BDD under quiescent conditions have been performed,<sup>10</sup> although the effect of sonication<sup>11,12</sup> and microwave activation<sup>13</sup> on the deposition process have been investigated. On the other hand, the deposition of PbO<sub>2</sub> from nitrate solutions on to glassy carbon electrodes has been extensively studied;<sup>14–21</sup> accordingly, nitrate solutions were used throughout experiments described below. The principal aims of this work were to investigate the cyclic voltammetric response of millimolar Pb(II) solutions at a range of acidic pH values on a boron-doped diamond (BDD) electrode, and to examine the changing morphology of the corresponding deposits by using in situ AFM (atomic force microscopy). Some previous attempts have been made to image the structure of PbO<sub>2</sub> electrodeposits formed under different conditions by using scanning electron microscopy (SEM) and scanning tunneling microscopy (STM);<sup>19,22–24</sup> however, this is the most wide-ranging study to date, encompassing PbO<sub>2</sub> deposition at acidic pH values between 7 and approximately 0 at a range of potentials. AFM has some significant advantages over SEM: for example, it allows the volume of suitably shaped deposits to be directly determined. Also, the fact that measurements may

be collected in situ allows the film properties to be measured as a function of time. However, it has disadvantages, mostly associated with the shape of the probe tip; the problems encountered when using AFM to image deposits such as those studied are therefore discussed in some detail. The catalytic activity of PbO<sub>2</sub> electrodes with respect to the oxidation of glucose<sup>25–28</sup> is also well-known, and is here exploited to correlate the activity of the films with their observed morphologies.

Boron-doped diamond (BDD) electrodes are commonly used in areas such as anodic stripping voltammetry, as the extreme flatness and hardness of the electrode surface provides potentially better reliability and reproducibility for analytical studies than for example glassy carbon electrodes (see Compton et al. and references therein).<sup>29</sup> BDD also allows use of a wider potential window. The same features that make BDD a useful analytical substrate also favor morphological studies; the flatness of the surface has previously been exploited in in situ AFM (atomic force microscopy) studies of growing lead nuclei,<sup>30</sup> in a manner similar to the work reported below.

## Experimental Section

All reagents were of analytical grade, used without further purification. The reagents used for making all nitrate-based solutions were the following: lead nitrate (BDH AnalaR, 99.5%+), nitric acid (Aldrich, 70%, AR grade), and potassium nitrate (BDH AnalaR, 99.5%). Glucose solutions were made with  $\alpha$ -D-glucose (Aldrich, A.C.S. grade). Solutions were prepared by using water with a resistivity of not less than 18.2 M $\Omega$  cm, using an Elgastat (Elga, Bucks, U.K.) UHQ grade water purification system. All measurements of pH were made with an Ag/AgCl glass combination electrode (BDH, Poole, Dorset,

\* To whom correspondence should be addressed. Phone: 01865 275413. Fax: 01865 275410. E-mail: richard.compton@chemistry.ox.ac.uk.

**TABLE 1: Composition of Solutions Used<sup>a</sup>**

soln	ca. HNO <sub>3</sub> concn/M	KNO <sub>3</sub> concn/M	measured pH
A	1.0	0	0.35
B	0.1	0	1.15
C	$1 \times 10^{-2}$	$9 \times 10^{-2}$	2.03
D	$1 \times 10^{-3}$	$9.9 \times 10^{-2}$	2.95
E	$1 \times 10^{-4}$	$9.99 \times 10^{-2}$	4.01
F	$1 \times 10^{-5}$	0.1	4.8
G	$1 \times 10^{-6}$	0.1	6.0
H	0	0.1	7.0

<sup>a</sup> In addition, each solution contained 2.5 mM Pb(NO<sub>3</sub>)<sub>2</sub>.

U.K.) in conjunction with a Jenway 3030 pH meter (Jenway Ltd., Dunmow, Essex, U.K.).

The boron-doped diamond (BDD) film used as the deposition electrode (having a working surface area of  $5 \times 5$  mm<sup>2</sup> and a thickness of 0.535 mm, with resistance approximately 0.4  $\Omega$ ) was grown on graphite by chemical vapor deposition and supplied by Element 6 (formerly DeBeers Industrial Diamond Division, Ascot, U.K.). It was pressed into a PTFE mounting, with an electrical connection made through the mount to a metal stub, using silver-loaded epoxy resin (RS). Before each measurement, the electrode was cleaned with 0.1  $\mu$ m monocrystalline diamond polishing compound (Kemet, Kent, UK), then thoroughly rinsed to remove any surface residue. In all experiments, a platinum wire was used as the counter electrode and a saturated calomel electrode (SCE, Radiometer, Lyon, France) as the reference electrode. All potentials reported in this paper are vs the SCE. A standard three-electrode configuration was used, controlled by a  $\mu$ Autolab type II potentiostat (Eco Chemie, Utrecht, The Netherlands). Ex situ deposition was performed in a cell having a volume of approximately 25 cm<sup>3</sup>, while a Digital Instruments fluid cell (with an approximate volume of 0.5 cm<sup>3</sup>) was used for all in situ experiments. A more detailed description of the use of this fluid cell is given elsewhere.<sup>30</sup>

All optical microscopy was performed with a Digital Instruments OMV-PAR microscope based on a Sony XC-999P CCD camera, having a maximum resolution of 752  $\times$  582 pixels over an area of 540  $\times$  400  $\mu$ m.

The AFM used was a Digital Instruments (now a division of Veeco) Multimode SPM, operating in fluid TappingMode. A model "J" scanner was used, having a lateral range of 125  $\times$  125  $\mu$ m and a vertical range of 5  $\mu$ m. Standard silicon nitride probes (Veeco part number NP), having a force constant of approximately 0.58 N m<sup>-1</sup>, were used.

## Results/Discussion

**1. Cyclic Voltammetry.** Eight solutions were prepared, each containing 2.5 mM Pb(NO<sub>3</sub>)<sub>2</sub> and varying concentrations of HNO<sub>3</sub> and KNO<sub>3</sub>. The compositions of the solutions used are shown in Table 1. The HNO<sub>3</sub> concentrations stated are approximate: to quantify the acidity of each solution, the pH was independently measured as described above (also shown in Table 1). Note that in all cases except solution A, the total nitrate concentration was maintained at 0.1 M. These solutions were used in the experiments described below. In neutral or acidic solution, the overall reaction for the generation of PbO<sub>2</sub> is



(although the elementary steps of this reaction are the subject of considerable debate).<sup>15,19,31–36</sup> It should be noted that the solutions used were unbuffered; the addition of buffer is known to affect the morphology of many electrodeposits, including PbO<sub>2</sub>.<sup>37</sup> It is therefore possible that during the experiments the

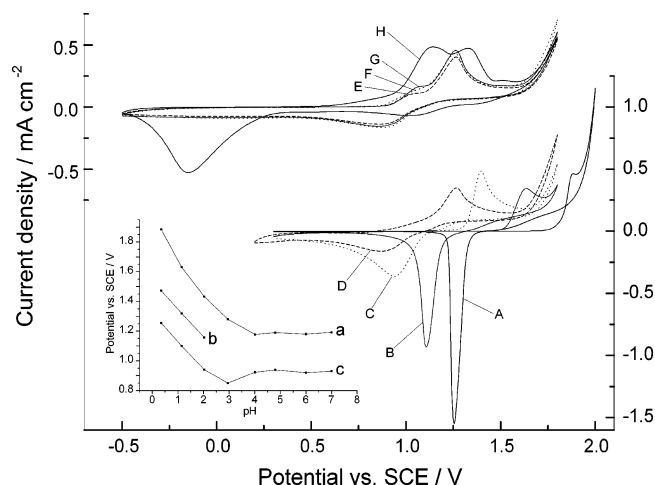


**Figure 1.** Steady state (10th scan) cyclic voltammetry of 2.5 mM Pb(NO<sub>3</sub>)<sub>2</sub> solutions recorded at 25 mV s<sup>-1</sup>. A–H refer to the solutions listed in Table 1. Note that the voltammograms have been staggered for clarity. Inset: Significant features of the CV data: (a) oxidation peak potential, (b) crossover potential (where applicable), and (c) reduction peak potential.

surface pH differed from the bulk pH to some extent. To avoid any significant pH shifts in the bulk solutions A–H (particularly those with low HNO<sub>3</sub> concentrations), the working solution was changed after each experiment.

Cyclic voltammetry was performed at 25 mV s<sup>-1</sup>, at potentials between -0.5 and up to +2.0 V for 10 cycles in each solution. The first scan in each case showed a nucleation loop, while successive cycling showed increasing current, probably due to deposited PbO<sub>2</sub> increasing the effective electrode surface area (see AFM section below). No significant shifts in peak potentials were observed on cycling. Solutions A–D (up to pH 2.95) showed a nucleation loop and subsequent crossover point on every scan, while solutions E–H (pH 4.8–7) showed a nucleation loop only on the first scan. After approximately 10 cycles the voltammetry had stabilized; the 10th scan in each case is shown in Figure 1, corresponding to the steady state. The following features are apparent: In solution H (pH 7), two oxidation peaks of similar size appear, along with two reduction peaks—one small peak at approximately 1.0 V, and a much more pronounced one at -0.25 V. At decreasing pH values, the first oxidation peak becomes smaller relative to the second until solution D (pH 2.95), where the first oxidation peak disappears. The reduction peak at -0.25 V becomes a broad plateau in solutions G and F, and is unidentifiable in solution E (pH 4.01). The other reduction peak becomes much sharper and better defined with decreasing pH. The potentials of the main oxidation and reduction peaks at each pH are shown in the inset to Figure 1, along with the crossover potential where applicable. From pH 0.35–2.03, all three points move to less positive potentials at a rate of approximately -180 mV per decade. At all higher pH values there is no significant change in the peak positions.

The voltammogram for solution A in Figure 1 may be compared to the results of Velayutham and Noel,<sup>20,21</sup> who performed an experiment in which PbO<sub>2</sub> was deposited from a solution containing 0.1 M Pb(NO<sub>3</sub>)<sub>2</sub> and 1 M HNO<sub>3</sub> on to a glassy carbon electrode. The resulting CV was qualitatively similar to that in Figure 1; a single oxidation peak was observed at approximately +1.6 V, and a single reduction peak at +1.2 V vs SCE. However, the signal was much less stable—the initially sharp reduction peak was found to decrease and broaden significantly over four cycles. In the present experiments, once

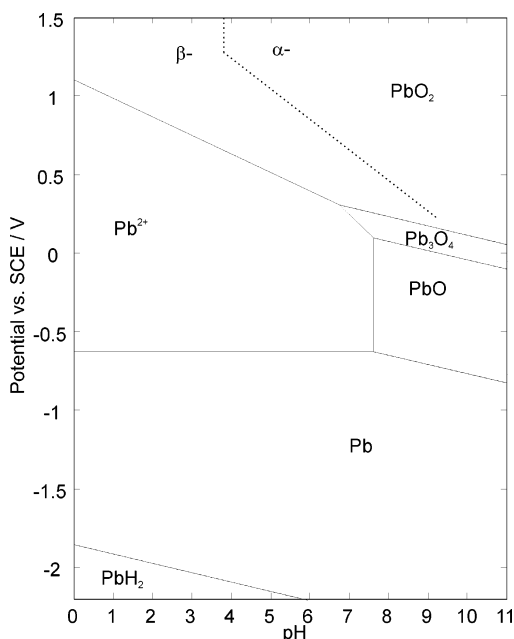
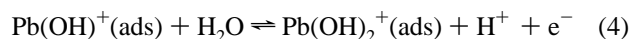
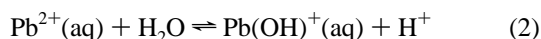


**Figure 2.** The simplified Pourbaix diagram for 2.5 mM lead in sulfate solution (drawn after Pourbaix et al.).<sup>39,40</sup> The approximate stability regions for  $\alpha$ - and  $\beta$ -PbO<sub>2</sub> are also shown, divided by a dashed line.<sup>45,46</sup>

the CV had stabilized, the size of the reduction peak remained roughly stable.

Also, the voltammogram for solution H in Figure 1 should be compared to the results of Hwang et al.,<sup>31</sup> who deposited PbO<sub>2</sub> on a Pt electrode from a 1 M Pb(NO<sub>3</sub>)<sub>2</sub> solution; they observed two oxidation peaks at +1.2 and +1.4 V and two reduction peaks at +0.91 and +0.36 V vs SCE. These data were interpreted by invoking an insoluble Pb(III) species immobilized on the electrode surface according to the following scheme (originally proposed without reaction 3 by Beck):<sup>38</sup>



in which the oxidation peak at +1.2 V corresponds to reaction 4, and the peak at +1.4 V to reaction 5. Another interpretation of the data shown in Figure 1 is suggested by the Pourbaix diagram for lead in sulfate solution (Figure 2).<sup>39,40</sup> In strongly acidic solutions, Pb<sup>2+</sup>(aq) can be oxidized directly to PbO<sub>2</sub>. The Pb<sup>2+</sup>/PbO<sub>2</sub> boundary potential decreases with increasing pH at a rate of ca. 118 mV per decade at 25 °C. At approximately pH 7, as the applied potential is increased, Pb<sub>3</sub>O<sub>4</sub> begins to be generated before further oxidation to PbO<sub>2</sub>. This suggests that the first oxidation peak observed at the less acidic potentials studied may correspond to the formation of Pb<sub>3</sub>O<sub>4</sub>, while the second corresponds to the generation of PbO<sub>2</sub> at all pH values. Similarly, the appearance of two reduction waves at higher pH may be associated with the intermediate formation of Pb<sub>3</sub>O<sub>4</sub>.

The use of in situ optical microscopy during potential cycling provides some support for this interpretation. If a solution similar to solution A (pH 0.35) but containing 25 mM Pb(NO<sub>3</sub>)<sub>2</sub> is used, as the potential reaches its maximum, a clearly visible

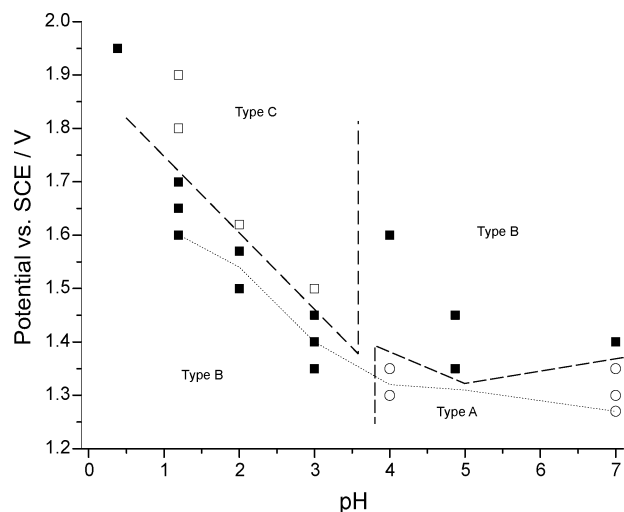


**Figure 3.** Potential/pH diagram showing the sets of conditions under which in situ AFM experiments were performed and the corresponding deposit morphology. Open circles: “type A”, spherical cap/hemispherical. Solid squares: “type B”, amorphous. Open squares: “type C”, amorphous. Dashed lines show approximate boundaries between the deposit types. The dotted line shows the oxidation peak potential.

black film ( $\beta$  lead dioxide) is formed, which then appears (at the resolution of the microscope) to be completely removed on the reverse scan. In a similar solution at pH 7.0, a thick layer of black lead dioxide is again deposited on the forward scan. However, on the reverse scan, the deposit turns red (probably Pb<sub>3</sub>O<sub>4</sub>) and a substantial amount remains at the lower scan limit. This observation also explains the different reverse-scan behavior between the acidic and less acidic solutions—in strong acid, a reverse loop is observed on every scan because the complete removal of the deposit requires re-nucleation. In weak acid, after the first scan, the nucleation sites remain filled, and no loop is observed. It is also interesting to compare these observations with the steady state voltammetry shown in Figure 1. In strongly acidic solutions (A–D) the total oxidation charge is similar to the charge of the first reduction peak, consistent with complete removal of the deposit on each reduction cycle. In solutions E–H the first reduction peak has a substantially lower charge than the oxidation peaks, consistent with the observation that the deposit is not removed under these conditions.

**2. In Situ AFM Morphology Analysis.** In situ AFM experiments were performed in a manner similar to that previously described,<sup>30</sup> using each of the solutions A–H. The electrochemical AFM cell was filled with the relevant solution, and the microscope engaged with the potentiostat at the open-circuit potential (OCP). With the scan rate set to 0 Hz (to minimize tip interference in the deposition process), a potential step was applied for a given time, then the potentiostat reset to the OCP. A 256-line scan was then collected at 3 Hz, and the process repeated as long as required (in practice, usually until the deposits grew to such a size that they became unstable and could not be reliably imaged due to tip smearing). The three variables for a given solution are scan size, time of deposition between scans, and deposition potential. For each solution, experiments were attempted at several deposition potentials, chosen such that the applied potential was initially somewhat lower than the potential of the PbO<sub>2</sub> deposition peak, and then increased in steps until the applied potential was significantly higher than the peak position. The precise potentials used are shown in Figure 3. Note that the potentials used do not necessarily correspond to the deposition peak positions in Figure



1; it was found that owing to the greater ohmic drop inside the AFM cell compared to the ex situ cell, peak deposition potentials moved by up to approximately +50 mV. However, the essential features of the voltammetry remained the same. For an experiment in a given solution and at a given potential, the step time and scan size were chosen by trial and error: at low potentials, longer step times were required to generate any detectable deposit, while less stable deposits could sometimes be imaged by decreasing the scan size (thereby reducing the tip velocity). In all cases, however, the step time was between 2 and 30 s, and the scan range between 5 and 20  $\mu\text{m}$ .

Each collected image was analyzed in four ways: the mean roughness ( $R_a$ , defined as the arithmetic mean of the absolute values of the surface height deviations measured from the mean plane) was calculated, along with the deposit surface area. The surface area of each scan was computed with Digital Instruments' Nanoscope software, employing a method based on summation of triangles defined within two-by-two pixel kernels over the surface to be analyzed. This surface area was then re-expressed as the proportion by which the measured surface area differed from that of a perfectly flat scan having the same scan size (hereafter referred to as the "percent surface area difference"). This conversion was used rather than the measured surface area to allow a reasonable comparison between scans of different sizes to be made. The total deposit volume (extrapolated to a scan size of 1  $\text{cm}^2$ , again to allow comparison between scans of different sizes) was also found. Finally, the morphology was classified according to the qualitative appearance of the deposits. These properties are discussed in detail below:

The morphological classification is of considerable interest, because over the pH and potential range studied three distinct deposit types were observed. These have been designated "types A–C". Type A deposits appear as separated, rounded, asymmetric square pyramids. Type B deposits are amorphous—they consist of irregularly sized, "lumpy" features, often poorly separated. Type C deposits appear to have a striking semiregular pyramidal shape. Examples of each of these are shown in Figure 4A–C, and the distribution of each type is shown in Figure 3. When analyzing AFM scans on scales such as those in Figure 4, it is important to remember that artifacts caused by the shape of the tip may significantly affect the appearance of the image, along with associated properties such as the apparent roughness and volume.<sup>41–43</sup> The relatively large scan sizes used mean that problems due to the precise shape and radius of the end of the tip are not an issue. However, Veeco-type NP probes have a square pyramidal tip with a half angle of 35° in all directions. The cantilever is mounted at 12° from the horizontal, giving effective tip half angles of 23° on the front face (in the forward scan direction) and 47° on the back face. As a result, any surface feature steeper than the tip angle at the point of contact will not image correctly, instead appearing as some feature of the tip; in the limit of an infinitely sharp point, an exact image of the tip itself will be generated.<sup>44</sup> Owing to the lack of rotational symmetry of the tip, it is difficult to visualize the exact effect such artifacts will have, even on relatively simple deposit shapes such as hemispheres. This problem may be overcome by the application of a simple model: using Matlab, two 256  $\times$  256 matrices were generated, one representing the "real" surface, the other the tip. The surface matrix was filled with height data (exactly the same as the manner in which Nanoscope height plots are stored). The point (128, 128) in the tip matrix was set to 0, while all other points were computed to have heights representing a square pyramid having specified side angles. The

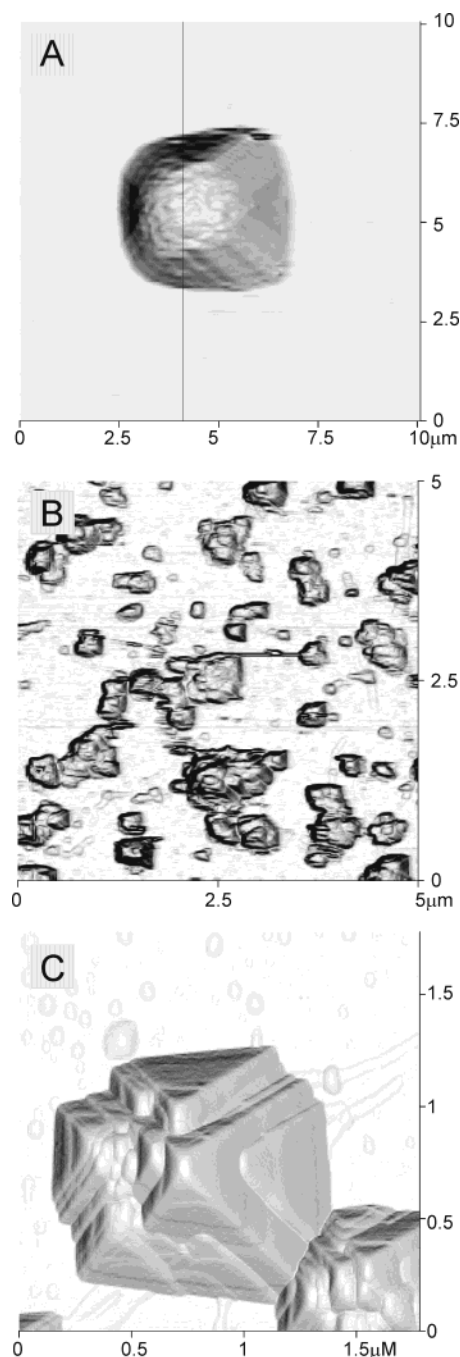


**Figure 4.** Examples of type A–C morphologies. The images are presented as illumination plots to enhance morphological detail: (A) deposited from solution E (pH 4) at +1.30 V for 180 s (feature height: approximately 1.5  $\mu\text{m}$ ); (B) solution E (pH 4), +1.6 V, 20 s (feature height: up to 300 nm); and (C) solution C (pH 2.03), +1.62 V, 60 s (feature height: approximately 500 nm).

tip matrix was then offset from the surface matrix such that the "point" of the tip successively appeared at the position of each entry on the surface matrix. At each offset, the tip matrix had a constant added to it equal to the height of the surface at the "tip point". The surface matrix was then subtracted from the tip matrix. If no values were negative, the height of the "real" surface was entered at the corresponding point in an output matrix. If any negative values were found, the largest was entered into the output matrix, equivalent to the real AFM tip being lifted by the contact between one of the tip sides and the real surface. After every point has been considered, the output matrix contains a list of heights as would be reported by an

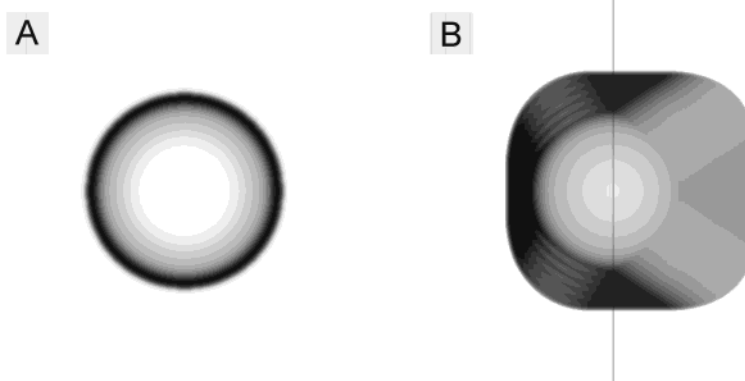


**Figure 5.** Effect of scanning a simulated AFM tip of dimensions similar to that of the tip used—a hemisphere (A) appears as the shape in part B. Compare this to Figure 4A.

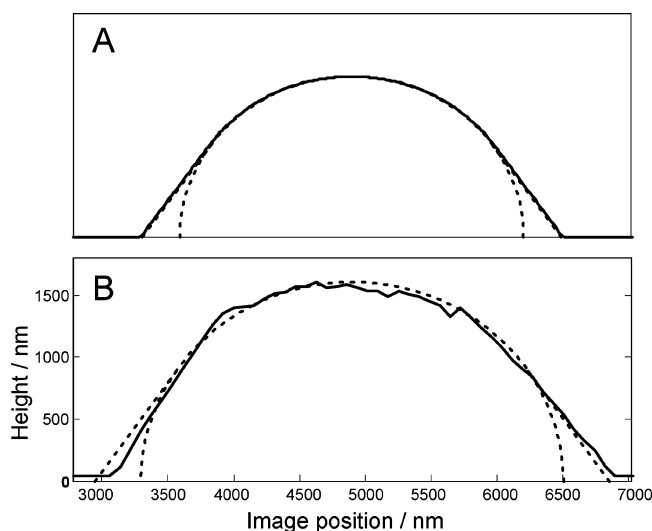


**Figure 6.** Cross-section plots of (A) the simulated deposit in Figure 5B and (B) the real deposit in Figure 4A. The point at which the section was measured is shown in those figures as black lines. Dotted lines show optimized fits to a real hemisphere, including artifacts from a 35° tip side angle.

AFM having tip angles the same as those of the tip matrix. The result of applying this method to a hemisphere is illustrated in Figure 5: we see a roughly square pyramidal shape, symmetric along the slow scan axis and asymmetric along the fast scan axis, with only the top of the hemisphere recovered correctly; comparison with the experimental image in Figure 4A shows a striking resemblance. Section analyses through the centers of the deposits along the slow scan axis of the two images (Figure 6) are also very similar, strongly suggesting that the type A deposits are in fact very good approximations to hemispheres. Some further comments on these deposits are required: within the “type A” pH/potential zone, the aspect ratio of the deposits is not entirely constant. At higher potentials, very good hemispheres such as those illustrated in Figure 4A are observed, while at the lowest potentials studied the deposits appeared more spherical cap shaped. Although generally contact angles could not be directly determined (as they were above 55°), estimates from the curvature of the tops of the caps suggested angles of 60–70°. By using the simulation, an estimate can also be made of the real volume of the deposits. For example, in the case of a perfect hemisphere, tip artifacts consistently increase the apparent volume by approximately 30%. The deposit volumes are discussed further below.

“Type B” deposits (Figure 4B), which appear at high potential at high pH values and low potential at low pH values, are

amorphous and have a low aspect ratio: no plane artifacts appear. They are variable in size, generally smaller and more densely packed at higher potential, and usually have roughly circular horizontal sections. The absence of tip artifacts implies that the AFM data may be used to compute deposit volumes with no correction.

“Type C” deposits (Figure 4C), which occur only in more acidic solutions at high potentials, appear as approximately square pyramidal shapes aligned with the scan axis—clearly a significant fraction of the AFM scan is due to tip artifacts. This is illustrated by considering the side angles of the feature in Figure 4C: 46° in the forward direction, 64° back, 49° up, and 61° down, indicating that the tip was engaged at about 9° from its axis in the horizontal direction and 6° in the vertical direction. It is apparent that much information about the structure of the deposit is irreversibly lost: simulations using simple “amorphous” surfaces generated by randomly positioning overlapping cuboids with their heights randomly generated then weighted according to distance from the image center, to create an irregular conical shape, again give results qualitatively very similar to the experimental scans (see Figure 7), and suggest that the true volume is overestimated by up to 40–50%. From the evidence available, it appears that type C deposits are amorphous, again probably with a roughly circular horizontal section, but have a much higher aspect ratio than type B deposits. They are also strongly adherent and relatively hard—little smearing was observed. Despite the general similarities of type B and C deposits, there is no smooth transition between the two. When deposition was performed in solution D (pH 2.95) at +1.45 V, we see an interesting mixture (shown in Figure 8): the two types have similar mean heights, but the difference in morphology is clear. At higher potentials, only type C is observed, while only type B is seen at lower potentials.

Overall, it is interesting to compare the distribution of morphologies shown in Figure 4 with the lead Pourbaix diagram (Figure 2). Shown on this diagram are the approximate stability regions for  $\alpha$ - and  $\beta$ -PbO<sub>2</sub>: the  $\beta$  polymorph dominates in highly acidic conditions, while the  $\alpha$  form dominates at high potential in less acidic conditions.<sup>45,46</sup> At large potentials, the division between the two areas occurs between pH 4 and 3, suggesting that the transition from type B deposits to type C may reflect a transition from  $\alpha$ - to  $\beta$ -PbO<sub>2</sub>.

Under sets of conditions where data could be obtained over a sufficiently long time (usually at least 60 s), the curves for the volume, surface area, and roughness of the deposits vs time showed an “s” shape, with an induction time followed by a steep increase, followed by a decrease in gradient. Note that this final decrease in gradient of the volume curve is not an artifact due

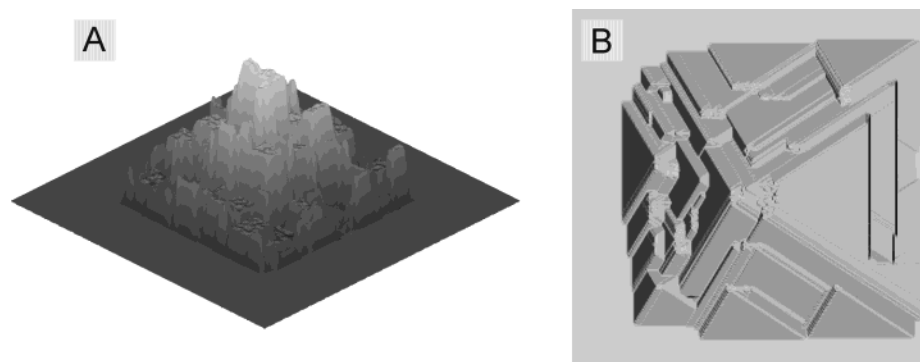


**Figure 7.** The effect of applying the tip artifact simulation procedure to an artificial irregular roughly conical feature: (A) the original artificially generated deposit (see text) and (B) the deposit after tip artifacts have been simulated. Compare this with Figure 4C.

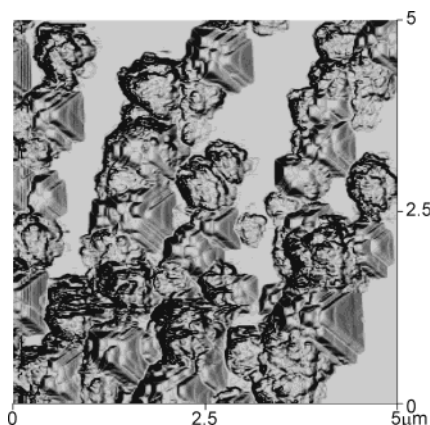


**Figure 8.** AFM image collected in solution D (pH 2.95) at +1.45 V, after 25 s. Note the clear mixture of type B and C morphologies. The largest deposits are approximately 500 nm high.

to deposit coalescence into a film—in all cases the experiments were stopped while a significant amount of the diamond surface was still visible, to allow a correct baseline to be used in the volume calculations. The data for pH 7 are shown in Figure 9, and illustrate features common to all the pH values studied: in general, applying a larger potential results in a larger rate of increase in each of the parameters, and at a given potential the shapes of the three curves tend to match quite well. Note that in Figure 9 and the discussion below, real volumes have been estimated for type A and C deposits, as described in the section above.  $R_a$  values and surface areas have not been altered, as it is not clear what a suitable correction factor would be; they therefore probably represent an overestimate.

There is no obvious model that can be applied to curves such as those in Figure 9, especially given that the deposits are generally amorphous but not uniformly so. To allow comparison between different pH values and potentials, the gradient of each volume curve was therefore arbitrarily calculated at the early approximately linear section (where possible). These gradients are plotted in Figure 10A. Although somewhat variable, a general trend appears: applying an increased potential increases the rate of growth, and for a given potential, the growth rate is generally higher at higher pH. Plots of  $R_a$  and percent surface area difference show trends very similar to those in Figure 10A; they are shown in Figure 10, parts B and C. This strong correlation is unsurprising: owing to the similar surface properties being used in the calculations, as long as there are fairly well separated features growing at some kind of smooth rate, the form of the three curves will be similar. Deviations would indicate the presence of a process such as film coalescence decreasing the surface area while the volume increases.

**3. Catalytic Activity of the  $\text{PbO}_2$  Surface.** To investigate the activity of the electrodeposited films with respect to the oxidation of glucose,  $\text{PbO}_2$  was deposited from solutions A–H as before under each of the sets of conditions shown in Figure 3. Deposition was continued until a charge of 40 mC had been transferred, to ensure a comparable deposit volume in each case. It should be noted that the resulting films were considerably thicker than those studied by AFM above; deposition required up to 1 h when lower potentials were applied. Clearly the “type A–C” classification used earlier is no longer directly applicable to such films. However, as is shown below, the boundaries at which the properties of the films deposited under different pH and potential conditions changed significantly were found to be approximately the same as those shown in Figure 3. After the  $\text{PbO}_2$  film had been formed, the electrode was removed from the solution, thoroughly rinsed, and placed in a solution containing 1 M  $\text{HNO}_3$ . Cyclic voltammetry was performed between +1.4 and +2.2 V at 50 mV  $\text{s}^{-1}$  for 5 cycles. The electrode was then transferred to a solution containing 1 M  $\text{HNO}_3$  and 100 mM glucose, and the cyclic voltammetry repeated. It was found that in all cases the voltammetry stabilized after 3–4 cycles; data from the fifth cycle were therefore used in the discussion below. Examples of the voltammograms recorded after deposition of  $\text{PbO}_2$  in solution B (pH 1.15) at +1.95 V are shown in Figure 11. We see the appearance of no new oxidation peaks, but an approximately 3-fold increase in the charge transferred between the bare BDD electrode in either solution and the  $\text{PbO}_2$ -deposited electrode in the base electrolyte, and a further 3-fold increase on transferring the  $\text{PbO}_2$ -deposited electrode to the glucose solution. The deposition followed by oxidation was found to be fairly reproducible: after polishing the BDD electrode and redepositing  $\text{PbO}_2$  under the same conditions as before, the observed charges differed from those in Figure 11 by less than 10%.

On platinum electrodes, the main product of glucose electrooxidation is gluconic acid.<sup>47,48</sup> The mechanism is thought to proceed via adsorption with dehydrogenation of glucose on the platinum surface at the carbon atom  $\text{C}_1$ .  $\text{OH(ads)}$  radicals are generated according to



Oxidation of the adsorbed glucose then proceeds via attack by the OH radical, to produce gluconic acid and water.<sup>47,48</sup>

The mechanism of glucose electrooxidation on  $\text{PbO}_2$  electrodes is less well understood. Unlike platinum,  $\text{PbO}_2$  does not have the ability to adsorb glucose via dehydrogenation of the active carbon atom. At the solution interface,  $\text{PbO}_2$  has been

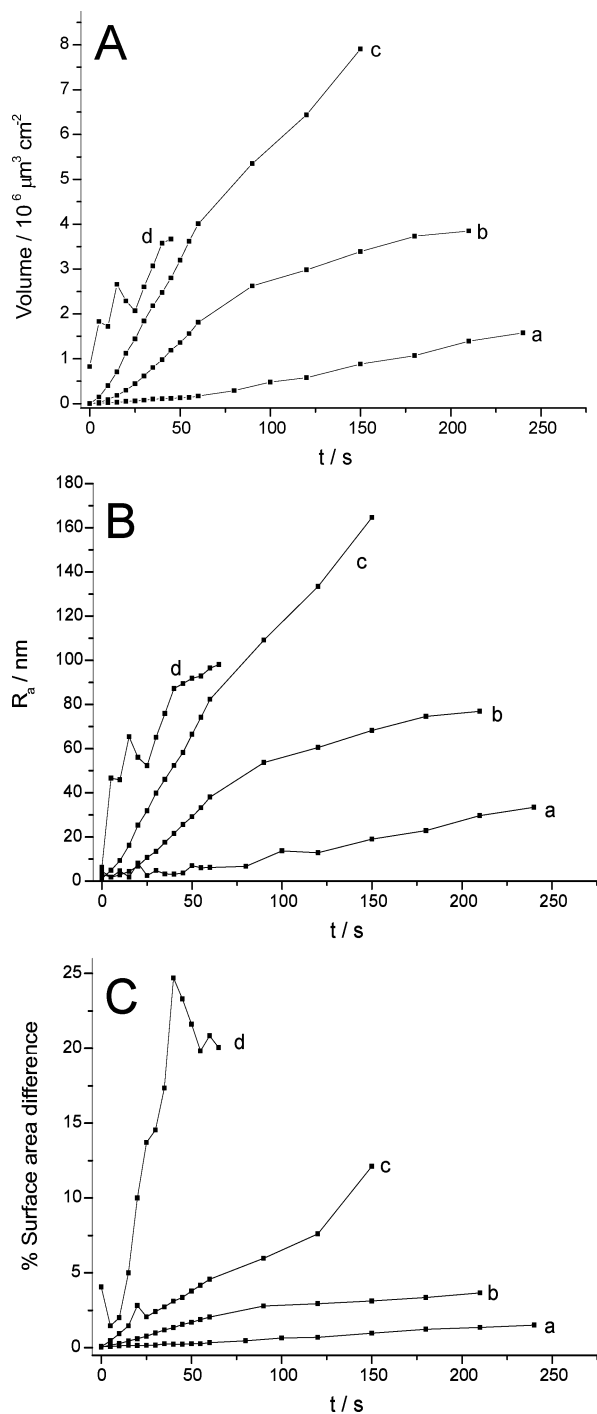
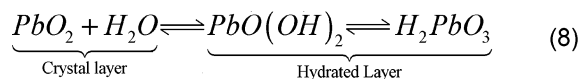


**Figure 9.** (A) Deposit volume, (B)  $R_a$ , and (C) percent surface area difference (see text for a description of these measurements) as a function of time, measured from in situ AFM images collected from solution H (pH 7). In each plot deposition was performed at (a) +1.27, (b) +1.30, (c) +1.35, and (d) +1.40 V.

shown to consist of a partially hydrated gel layer,<sup>49–51</sup> generated by the following equilibrium process:



This hydrated layer consists of polymer chains,<sup>52,53</sup> schematically presented in Figure 12. In the absence of oxidizable species in the solution, applying a sufficient positive potential to the electrode generates  $O_2$ . The exact mechanism of this process is debatable,<sup>1,2,54,55</sup> and possibly rather complex, involving the

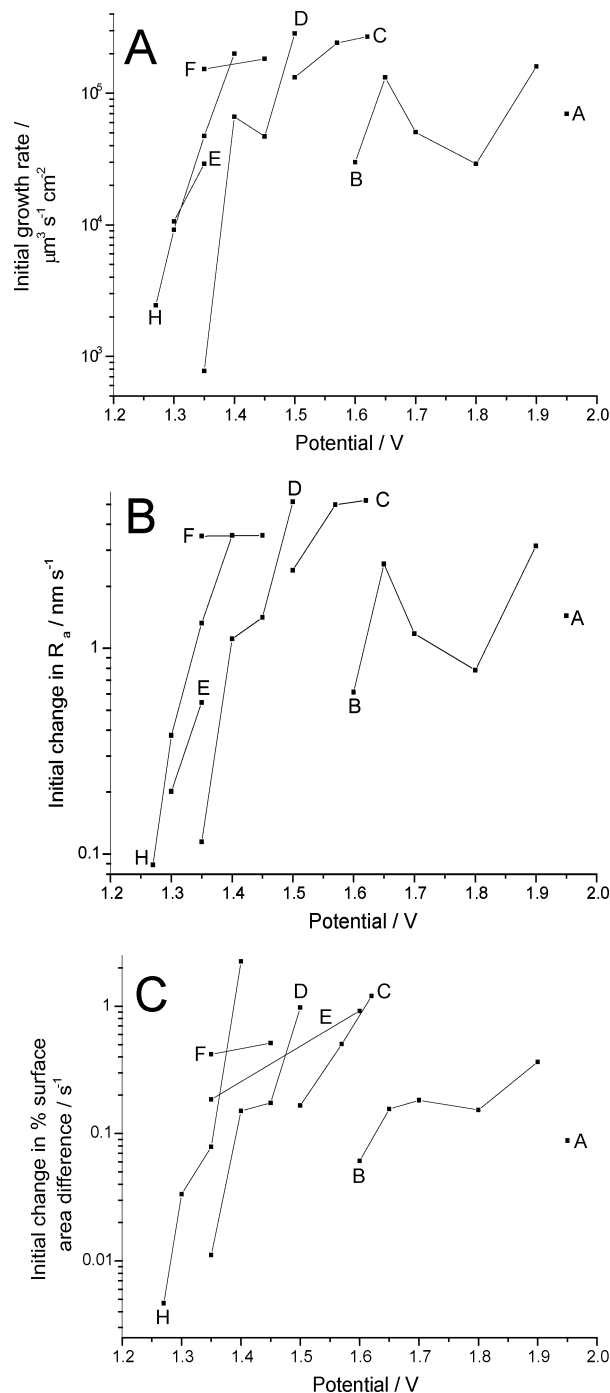
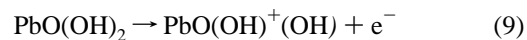


**Figure 10.** Initial (A) volume, (B)  $R_a$ , and (C) percent surface area difference growth rates as a function of applied potential, extracted from data such as that in Figure 9. A–H refer to the solutions described in Table 1.

creation of OH radicals associated with a limited number of active Pb centers in the polymer layer:<sup>49–51</sup>



where “...” indicates a weak bond between the Pb center and the OH radical. It is generally agreed that the electrochemically generated adsorbed OH radicals are relatively immobile, and their recombination to form  $O_2$  and water is therefore slow, resulting in a preequilibrium of OH radicals.



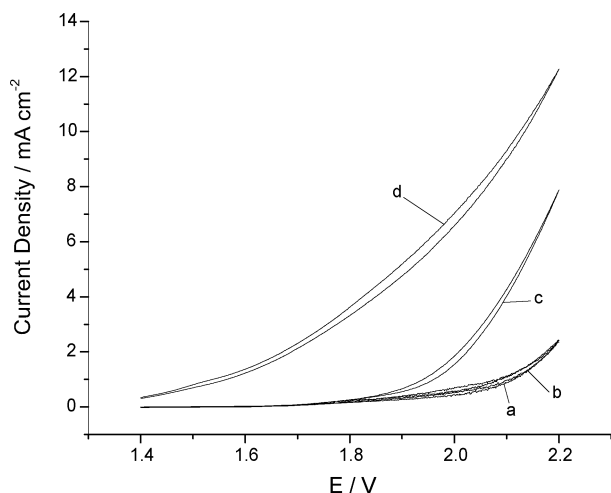


**Figure 11.** Cyclic voltammograms recorded between +1.4 and +2.2 V at 50 mV s<sup>-1</sup>, under the following conditions: (a) clean BDD electrode in 1 M HNO<sub>3</sub>, (b) clean BDD electrode in 1 M HNO<sub>3</sub> and 100 mM glucose, (c) BDD electrode after deposition from solution A (at +1.75 V until 40 mC of charge had been transferred) in 1 M HNO<sub>3</sub>, and (d) BDD electrode modified as in part (c), in 1 M HNO<sub>3</sub> and 100 mM glucose.

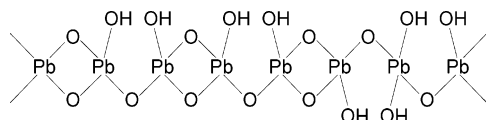
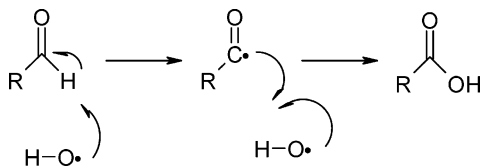


**Figure 12.** Schematic diagram of the structure of the hydrated polymer chains at the PbO<sub>2</sub>/aqueous interface.<sup>49</sup>

On addition of glucose to the solution, the OH radicals attack the aldehyde hydrogen of the  $\gamma$ -form of the glucose:



This process is probably further accelerated by the coordination of the aldehyde oxygens to Pb<sup>IV</sup> centers, increasing the local concentration of glucose at the hydrated layer surface.<sup>26</sup> The removal of OH radicals from the Pb active centers promotes reactions 9 and 10 (or more generally, reaction 7), resulting in the observed increase in oxidation current. It should be noted Bonfatti et al.<sup>26</sup> detected various products after bulk electrolysis of glucose in 2 M H<sub>2</sub>SO<sub>4</sub> solution including gluconic acid, glucaric acid, glucuronic acid, and arabinose, as well as other minor products, indicating that further oxidation is possible. Arabinose was a major product, implying that a Kolbe-like decarboxylation occurs after the initial oxidation in many cases; however, this should have no effect on the observed oxidation currents.

The total charges in base electrolyte and glucose solution observed under each set of conditions are plotted as a function of pH and PbO<sub>2</sub> deposition potential in Figure 13, parts A and B, respectively. Several trends are apparent: at pH values of 3 and above, increasing the deposition potential increases the resulting glucose oxidation charge, while at more acidic pH values the deposition potential appears to have much less relative effect on the oxidation charge. This change in behavior occurs between pH 3 and 2, close to (although more acidic than) the pH boundary between type A/B and B/C deposits, again suggesting a change from  $\alpha$ - to  $\beta$ -PbO<sub>2</sub>. A possible explanation

for the trends at pH 3 and above is simply that the films deposited at higher potentials have larger surface areas: although not directly comparable owing to the different conditions under which the data were collected, the trends shown in Figure 10C show that the rate of increase of the surface area of films deposited is greater at higher potentials. Below pH 3 the deposition potential has a much less pronounced effect—in fact, the charges are more or less independent of PbO<sub>2</sub> deposition potential.

The ratio of total oxidation charges to charges in base electrolyte are plotted as a function of pH and PbO<sub>2</sub> deposition potential in Figure 13C. We find that at any given pH (except pH 0), as the PbO<sub>2</sub> deposition potential increases, the ratio decreases until the type A/B or type B/C potential boundary is reached. Upon crossing the potential boundary, there is an increase in the ratio. The base electrolyte charges show trends similar to the total charges (Figure 13, parts A and B), implying that higher PbO<sub>2</sub> deposition potentials promote the generation of OH radicals. The decrease in relative total oxidation charge sizes suggests that the rate of removal of these radicals by glucose decreases; however, the reason for this is not clear.

## Conclusions

The deposition of PbO<sub>2</sub> from 2.5 mM lead(II) nitrate solutions at pH values between approximately 0 and 7 has been studied by three complementary methods: cyclic voltammetry, in situ AFM, and analysis of the film catalytic activity with respect to the oxidation of a 100 mM glucose solution in 1 M HNO<sub>3</sub>.

With use of cyclic voltammetry, it was shown that a mechanism change occurs between approximately pH 3 and 4. Below pH 4, one oxidation peak and one reduction peak are observed, with the position of each peak dependent on pH. The reversibility of the process decreases with increasing pH: the reduction peak broadens and flattens until at pH 3 it stabilizes as a broad plateau at approximately +1.0 V. Between pH 7 and 3, two oxidation peaks (and no crossover) are observed, the first of which becomes larger than the second at pH 7. This change in the form of the voltammogram is explained by consideration of the stability of the various forms of lead at different pH values and potentials;<sup>39</sup> it is suggested that the second oxidation peak at less acidic pH values corresponds to the formation of Pb<sub>3</sub>O<sub>4</sub> as an intermediate.

In situ AFM was used to observe the morphology and properties of PbO<sub>2</sub> deposits as a function of time during potentiostatic deposition at pH values between 0 and 7. Three distinct morphologies were observed: “Type A”, in which the deposits are hemispherical or spherical cap shaped, occurs at high pH and low potential. “Type B”, an amorphous deposit having a low profile, is found at high pH and high deposition potential and also low pH and low potential. Finally, “type C”, an amorphous deposit having a high profile that leads to distinctive AFM artifacts, appears at low pH and high potential. There is a quite distinct boundary between the sets of conditions resulting in each morphology (Figure 3), and the growth rate, surface area, and roughness of the films is also found to be dependent on the deposition conditions.

This differentiation between the deposit types suggested that they may also possess different catalytic properties. This supposition was tested by generating films under each set of conditions, then using them to oxidize a 100 mM glucose solution, as described above. Several important features are observed. First, simply depositing PbO<sub>2</sub> results in a large increase in oxidation current in a 1 M HNO<sub>3</sub> solution, owing to the catalytic generation of oxygen. This current increases



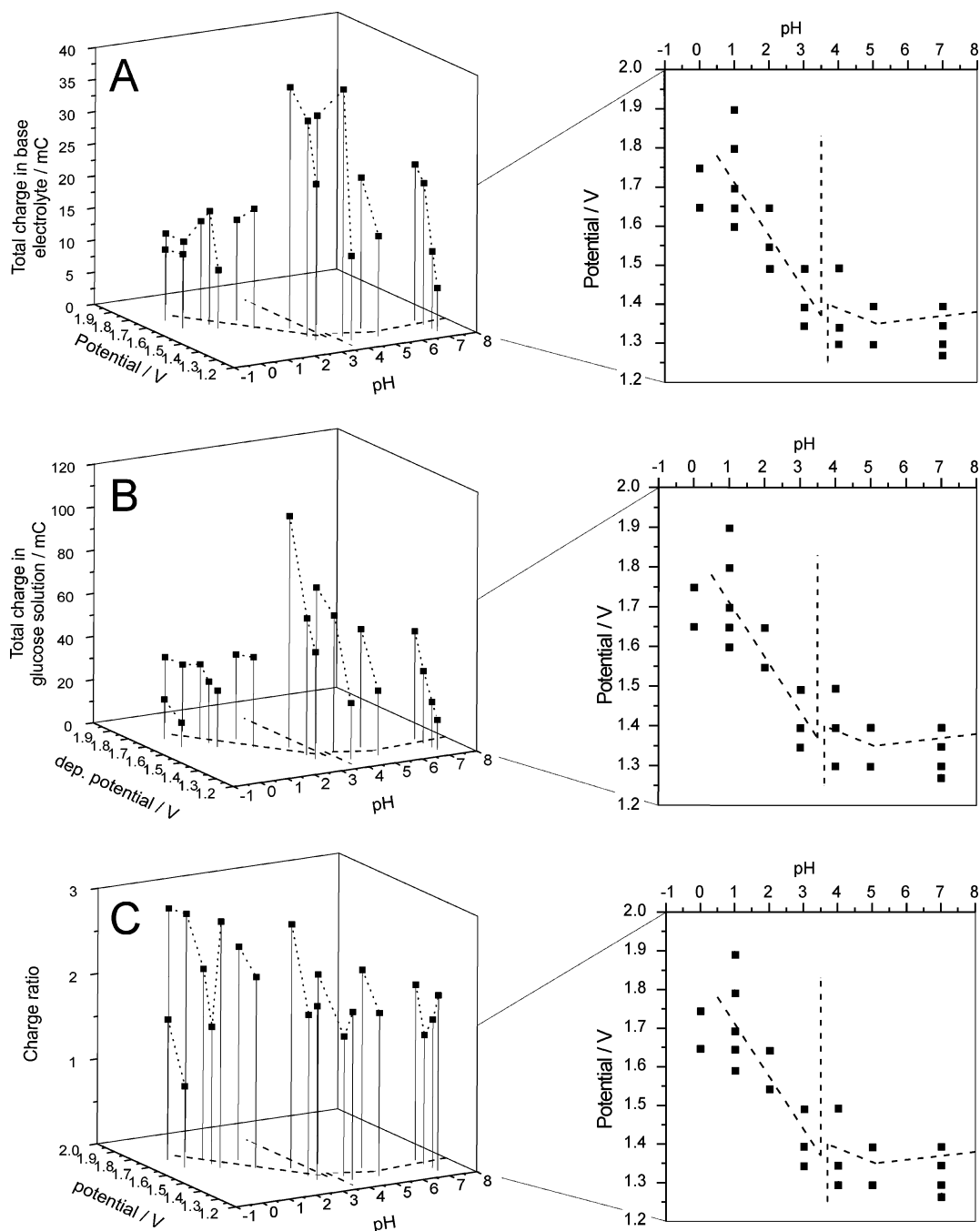


**Figure 13.** Charges transferred during cyclic voltammograms such as those illustrated in Figure 11, displayed as a function of  $\text{PbO}_2$  deposition potential and pH. (A) CVs recorded in 1 M  $\text{HNO}_3$  solution, (B) CVs recorded in 1 M  $\text{HNO}_3$  and 100 mM glucose, and (C) ratios of the charges observed in the glucose solution to the solution of base electrolyte. In all cases the dashed lines show the approximate boundaries between morphology types, as shown in Figure 3.

further on the addition of glucose. The first step in both processes is the generation of OH radicals (reactions 9 and 10), as a preequilibrium process. The further increase in current therefore implies that glucose accelerates the rate of removal of OH radicals bound to the  $\text{PbO}_2$  surface. Apart from these major effects, some interesting trends are observed. At pH 3 and above, increasing the  $\text{PbO}_2$  deposition potential usually increases the current in both the base electrolyte and glucose solutions. However, at more acidic pH values, this effect is much less pronounced—the currents are roughly independent of potential. When the glucose charges are expressed as a ratio of the charge in the base electrolyte solution, however, an unusual trend appears at all studied pH values. The ratio decreases with increasing deposition potential until the type A/B or type B/C

boundary is reached, then increases again. The reason for this is not obvious, but it clearly illustrates that the interesting differences in  $\text{PbO}_2$  morphology found under different deposition conditions have fundamental effects on the electrochemical behavior of the deposit.

## References and Notes

- (1) Ho, J. C. K.; Tremiliosi Filho, G.; et al. *J. Electroanal. Chem.* **1994**, 366, 147.
- (2) Feng, J.; Johnson, D. C.; et al. *J. Electrochem. Soc.* **1994**, 141, 2708.
- (3) Treimer, S. E.; Feng, J.; et al. *J. Electrochem. Soc.* **2001**, 148, E459.
- (4) Abaci, S.; Pekmez, K.; et al. *J. Appl. Polym. Sci.* **2003**, 87, 599.
- (5) Abaci, S.; Tamer, U.; et al. *J. Appl. Electrochem.* **2002**, 32, 193.

- (6) Amadelli, R.; De Battisti, A.; et al. *Electrochim. Acta* **2000**, *46*, 341.
- (7) Belhadj Tahar, N.; Savall, A. *J. Appl. Electrochem.* **1999**, *29*, 277.
- (8) Wu, Z.; Zhou, M.; et al. *Chemosphere* **2002**, *48*, 1089.
- (9) Johnson, D. C.; Feng, J.; et al. *Electrochim. Acta* **2000**, *46*, 323.
- (10) Yasuhisa, M.; Takayoshi, H.; et al. *Hyomen Gijutsu* **2003**, *54*, 64.
- (11) Saterlay, A. J.; Agra-Gutierrez, C.; et al. *Electroanalysis* **1999**, *11*, 1083.
- (12) Saterlay, A. J.; Wilkins, S. J.; et al. *J. Electrochem. Soc.* **2001**, *148*, E66.
- (13) Marken, F.; Tsai, Y.; et al. *J. Solid State Electrochem.* **2001**, *5*, 313.
- (14) González-García, J.; Gallud, F.; et al. *New J. Chem.* **2001**, *25*, 1195.
- (15) González-García, J.; Gallud, F.; et al. *J. Electrochem. Soc.* **2000**, *147*, 2969.
- (16) González-García, J.; Gallud, F.; et al. *Electroanalysis* **2001**, *13*, 1258.
- (17) González-García, J.; Iniesta, J.; et al. *New J. Chem.* **1998**, *4*, 343.
- (18) González-García, J.; Sáez, V.; et al. *Electrochem. Commun.* **2002**, *4*, 370.
- (19) Ramamurthy, A. C.; Kuwana, T. *J. Electroanal. Chem.* **1982**, *135*, 243.
- (20) Velayutham, D.; Noel, M. *Electrochim. Acta* **1991**, *36*, 2031.
- (21) Velayutham, D.; Noel, M. *Electroanalysis* **1991**, *6*, 157.
- (22) Shen, P. K.; Wei, X. L. *Electrochim. Acta* **2003**, *48*, 1743.
- (23) Li, L. J.; Fleischmann, M.; et al. *Electrochim. Acta* **1989**, *34*, 459.
- (24) Sexton, B. A.; Cotterill, G. F.; et al. *J. Vac. Sci. Technol. A* **1990**, *8*, 544.
- (25) Bonfatti, F.; Ferro, S.; et al. *J. Electrochem. Soc.* **1999**, *147*, 592.
- (26) Bonfatti, F.; Ferro, S.; et al. *J. Electrochem. Soc.* **1999**, *146*, 2175.
- (27) Ho, C. C.; Chan, C. Y.; et al. *J. Chem. Technol. Biotechnol.* **1986**, *36*, 7.
- (28) Gorski, W.; Kennedy, R. T. *J. Electroanal. Chem.* **1997**, *424*, 43.
- (29) Compton, R. G.; Foord, J. S.; et al. *Electroanalysis* **2003**, *15*, 1349.
- (30) Hyde, M. E.; Jacobs, R.; et al. *J. Phys. Chem. B* **2002**, *106*, 11075.
- (31) Hwang, B. J.; Santhanam, R.; et al. *Electroanalysis* **2002**, *14*, 363.
- (32) Chang, H.; Johnson, D. C. *J. Electrochem. Soc.* **1989**, *136*, 17.
- (33) Chang, H.; Johnson, D. C. *J. Electrochem. Soc.* **1989**, *136*, 23.
- (34) Velichenko, A. B.; Girenko, D. V.; et al. *J. Electroanal. Chem.* **1996**, *405*, 127.
- (35) Fleischmann, M.; Liler, M. *Trans. Faraday Soc.* **1958**, *54*, 1370.
- (36) Campbell, S. A.; Peter, L. M. *J. Electroanal. Chem.* **1991**, *306*, 185.
- (37) Thanos, J. C. G.; Wabner, D. W. *J. Electroanal. Chem.* **1985**, *182*, 37.
- (38) Beck, F. *J. Electroanal. Chem.* **1975**, *65*, 231.
- (39) Pourbaix, M. *Atlas of electrochemical equilibria in aqueous solutions*; Pergamon Press: Oxford, UK, 1966.
- (40) Delahay, P.; Pourbaix, M.; et al. *J. Electrochem. Soc.* **1951**, *98*, 57.
- (41) Maurice, P. A. *Colloids Surf. A* **1996**, *107*, 57.
- (42) Griffith, J. E.; Grigg, D. A. *J. Appl. Phys.* **1993**, *74*, R83.
- (43) Westra, K. L.; Thomson, D. J. *J. Vac. Sci. Technol. B* **1995**, *13*, 344.
- (44) Oden, P. I.; Nagahara, L. A.; et al. *Ultramicroscopy* **1992**, *42–44*, 580.
- (45) Burbank, J. *J. Electrochem. Soc.* **1957**, *104*, 693.
- (46) Dawson, J. L. In *The Electrochemistry of Lead*; Kuhn, A. T., Ed.; Academic Press: London, UK, 1979.
- (47) Vassilyev, Y. B.; Khazova, O. A.; et al. *J. Electroanal. Chem.* **1985**, *196*, 105.
- (48) Vassilyev, Y. B.; Khazova, O. A.; et al. *J. Electroanal. Chem.* **1985**, *196*, 127.
- (49) Pavlov, D.; Monahov, B. *J. Electrochem. Soc.* **1996**, *143*, 3616.
- (50) Pavlov, D.; Balkanov, I.; et al. *J. Electrochem. Soc.* **1989**, *136*, 3189.
- (51) Monahov, B.; Pavlov, D. *J. Appl. Electrochem.* **1993**, *23*, 1244.
- (52) Pavlov, D. *J. Electroanal. Chem.* **1992**, *139*, 3075.
- (53) Pavlov, D.; Balkanov, I. *J. Electrochem. Soc.* **1992**, *139*, 1830.
- (54) Pavlov, D.; Monahov, B. *J. Electrochem. Soc.* **1998**, *145*, 70.
- (55) Amadelli, R.; Maldotti, A.; et al. *J. Electroanal. Chem.* **2002**, *534*, 1.